



Cite this: *J. Mater. Chem. A*, 2025, **13**, 29109

Achieving superior stability and cycle life in zinc anodes with aramid surface modification

Ayoung Kim,^a Heejin Kim ^{*b} and Kwan Woo Nam ^{*a}

Aqueous zinc-ion batteries (AZIBs) are promising alternatives to lithium-ion battery systems for large-scale energy storage, offering safety, material abundance, and environmental advantages. However, Zn metal anodes face significant challenges, including dendritic growth and side reactions, limiting their cycling stability. In this investigation, we present an aramid-based polymer coating engineered to address these issues by promoting uniform Zn deposition, suppressing side reactions, and enhancing resistance to thermal stress. Electrochemical impedance spectroscopy (EIS) results demonstrate a notable reduction in charge transfer resistance (R_{ct}) in the Aramid@Zn configuration, and X-ray diffraction (XRD) analyses reveal minimal formation of corrosion-related by-products. Symmetric cell cycling results confirm the superior durability of Aramid@Zn, showing stable cycling beyond 1000 hours at 1 mA cm^{-2} . When applied in $\text{Zn}||\alpha\text{-MnO}_2$ full cells, the Aramid@Zn anode exhibits a capacity retention of 80.2% after 2000 cycles at 1 A g^{-1} , outperforming its Bare Zn counterparts. These results underscore the aramid layer's role in promoting a stable interfacial structure and inhibiting dendritic growth, offering a robust strategy for enhancing AZIB stability.

Received 16th May 2025
Accepted 4th August 2025

DOI: 10.1039/d5ta03948g
rsc.li/materials-a

Introduction

Lithium-ion batteries (LIBs) are widely recognized for their high energy density and cycle stability, making them an ideal energy storage system. These properties have led to their application in grid-level energy storage systems, where they provide rapid response, modularization, and flexible installation.¹ However, the toxic, flammable, and environmentally unfriendly nature of the organic electrolyte used in LIBs has hindered their application in large-scale energy storage systems (ESSs).²⁻⁴ Aqueous zinc-ion batteries (AZIBs) have emerged as a next-generation alternative to LIBs for ESSs owing to their safety, abundance of materials, and eco-friendliness.^{5,6} The Zn metal is considered one of the most promising anode candidates for AZIBs due to its intrinsic safety, high theoretical capacity (820 mAh g^{-1}), and low redox potential (-0.762 V vs. standard hydrogen electrode).^{7,8} Owing to these advantages, AZIBs have attracted growing research interest in recent years.⁹⁻¹³

Despite these positive attributes, Zn anodes in AZIBs have inherent challenges, including dendrite growth and side reactions.^{14,15} During continuous Zn stripping/plating, the preferential deposition of Zn^{2+} ions on uneven Zn metal surfaces leads to dendrite growth, a common issue in Zn anodes.¹⁶ These dendrites can easily penetrate the separator and bridge the

electrodes, causing internal short-circuits. In addition, side reactions such as self-corrosion produce an uneven Zn surface and passivation layers, resulting in increased polarization. Furthermore, the hydrogen evolution reaction (HER) generates by-products such as zincate ($\text{Zn}(\text{OH}_4)^{2-}$), which contribute to poor cycling stability in AZIBs.

In order to address the challenges of dendrite growth and side reactions on Zn anodes, protective coatings have been developed to promote uniform Zn deposition and reduce parasitic reactions. Among these, polymer-based coatings have demonstrated significant potential due to their ability to create stable interfaces and inhibit dendrite formation. However, conventional polymers often limit Zn^{2+} ion access, increasing overpotential.¹⁷ In this investigation, an aramid-based polymer coating, rich in polar amide groups ($-\text{CONH}-$), has been engineered to form an artificial solid electrolyte interphase (SEI) on the Zn surface. The aramid layer promotes uniform Zn^{2+} distribution and smooth deposition, acting as a barrier to electrolyte contact while enabling efficient ion transport. This coating not only supports even Zn deposition but also enhances interfacial stability, reducing dendrite formation and suppressing side reactions. Additionally, the inherent thermal stability of the aramid layer helps maintain the structural and electrochemical integrity of the Zn anode, even under elevated temperature conditions.

During charge/discharge cycles, batteries typically generate significant Joule heat, leading to localized high temperatures that pose a safety risk.^{18,19} Given the high energy and power output of AZIBs, managing heat generation is critical to prevent

^aDepartment of Chemical Engineering and Materials Science, Graduate Program in System Health Science and Engineering, Ewha Womans University, Seoul 03760, Republic of Korea. E-mail: kwanwoo@ewha.ac.kr

^bDivision of Analytical Science, Korea Basic Science Institute, 169-148 Gwahak-ro, Daejeon, Republic of Korea. E-mail: heejinkim@kbsi.re.kr



performance degradation and ensure safe operation. External factors such as extreme temperatures, mechanical stress, or electrical misuse can exacerbate these risks by triggering thermal runaway,²⁰ highlighting the need for robust thermal stability in battery design. The aramid coating addresses these challenges by demonstrating excellent thermal stability, preserving the structural and electrochemical integrity of the Zn anode even under elevated temperature conditions, which normally accelerate Zn corrosion and dendrite growth.²¹ Such temperatures, arising from increased internal resistance and electrochemical reactions during cycling, contribute to performance degradation by promoting hydrogen gas evolution and the formation of non-conductive by-products on the Zn surface. Under these conditions, the Aramid@Zn anode effectively suppresses Zn corrosion, minimizes dendrite growth, and reduces interfacial resistance, thereby significantly enhancing the stability and durability of the Zn anode.

Herein, the effectiveness of the aramid coating is verified through symmetric cell tests, where the Aramid@Zn anode maintains stable cycling over 1000 h at a current density of 1 mA cm^{-2} . The aramid layer also effectively mitigates side reactions, as evidenced by reduced by-product formation and enhanced corrosion resistance. When paired with an $\alpha\text{-MnO}_2$ cathode, the Aramid@Zn|| $\alpha\text{-MnO}_2$ full cell exhibits excellent cycling stability over 2000 cycles, with high capacity retention. This enhanced interfacial stability highlights the potential of the Aramid@Zn anode to improve the durability and reliability of advanced AZIBs.

Results and discussion

Inhibition of side reactions

Fig. 1 shows a schematic diagram illustrating the inhibition of Zn dendrite formation and side reactions by aramid coating. During cycling in ZnSO_4 solution, Zn^{2+} ions are unevenly deposited on the exposed Bare Zn metal surface, resulting in dendrite formation. Additionally, self-corrosion and HER compromise the Zn electrode, producing OH^- ions that lead to by-products such as $\text{Zn}_4\text{SO}_4(\text{OH})_6 \cdot x\text{H}_2\text{O}$ (ZSH). In contrast, the aramid coated Zn electrode promotes a dehydration process, facilitating uniform Zn^{2+} deposition. The amide groups ($-\text{CONH}-$) in the aramid structure, identified *via* Fourier transform infrared spectroscopy (FT-IR) (Fig. S1, SI), provide the efficient Zn^{2+} ion transport pathways, effectively mitigating dendrite formation and suppressing HER and corrosion. As confirmed in Fig. S1(SI), the aramid chemical structure exhibits characteristic benzene-related vibrations, including aromatic C–H stretching, C–H bending, and C=C stretching, along with amide-specific bands such as carbonyl ($\text{C}=\text{O}$) and C–N stretching, clearly indicating the presence of aramid functional groups. The sharp XRD peak at $2\theta \approx 21^\circ$, as shown in Fig. S2(SI), confirms the para-aramid structure of the synthesized material.²² Consequently, the aramid layer significantly enhances the cycling stability of the Zn electrode by promoting uniform deposition and reducing side reactions.

Linear sweep voltammetry (LSV) was conducted to evaluate the ability of the aramid layer to inhibit HER (Fig. 2a). The LSV

curves demonstrate that the Aramid@Zn anode exhibits a significantly lower current density compared to the Bare Zn anode, indicating that the aramid coating effectively suppresses H_2 gas release. Corrosion behavior was further investigated *via* linear polarization tests (Fig. 2b). The Aramid@Zn anode demonstrates a more positive corrosion potential ($E_{\text{corr}} = -0.01 \text{ V}$) than Bare Zn ($E_{\text{corr}} = -0.03 \text{ V}$), reflecting its reduced susceptibility to corrosion. In addition, the corrosion current density (I_{corr}) of Aramid@Zn anode is significantly lower (0.33 mA cm^{-2}) compared to Bare Zn (1.25 mA cm^{-2}), illustrating its enhanced corrosion resistance by preventing HER associated side reactions.

To further investigate the stability of the Aramid@Zn coating, both Aramid@Zn and Bare Zn electrodes were immersed in ZnSO_4 electrolyte for 7 days. X-ray diffraction (XRD) analysis (Fig. 2c) confirmed the formation of by-products on the Zn anode surface. The primary by-product identified was $\text{Zn}_4\text{SO}_4(\text{OH})_6 \cdot x\text{H}_2\text{O}$ (ZSH), a brittle and rough compound formed due to HER and a localized pH increase.²³ The Bare Zn anode showed a significant peak attributed to ZSH, indicating severe corrosion induced by the aqueous electrolyte, whereas the Aramid@Zn anode exhibited negligible peak intensity. As observed in Fig. 2d, the surface of the Aramid@Zn anode exhibits only small amounts of ZSH, whereas the Bare Zn presents a noticeably rough surface covered with flake-like by-products.^{24,25} These results underscore the protective role of the aramid coating in preventing by-product formation. Digital images (Fig. 2e) further corroborate these findings, showing that after 7 days of immersion in the electrolyte, the Zn metal surface shows pronounced roughness and a loss of its characteristic metallic luster, indicating a significant reduction in resistance to side reactions. Conversely, the aramid coated Zn metal retained much of its initial appearance, demonstrating its ability to effectively resist side reactions. To further validate the by-product inhibition, optical microscopy (OM) analysis was conducted after immersing the anode in electrolyte for 1, 2, and 7 days (Fig. S3, SI). The Bare Zn surface gradually became rough and opaque, indicating the accumulation of by-products. In contrast, the Aramid@Zn surface remained smooth and uniform throughout, supporting its role in suppressing parasitic reactions and facilitating homogeneous Zn deposition.

Properties and role of aramid layer

To serve as an effective artificial solid-electrolyte interphase (SEI), the surface coating layer must be both an ionic conductor and an electronic insulator. To verify this, the electrical and ionic conductivities of the aramid coating layer were examined. First, the aramid coating exhibits superior electrical resistivity, with a calculated value of $9.45 \times 10^3 \Omega \text{ cm}$ (Fig. S4, SI), confirming its effectiveness as an insulator at the Zn metal interface. This high electrical resistivity prevents undesired electron transfer through the aramid layer contributing to improved chemical stability.²⁶

The ionic conductivity was measured using electrochemical impedance spectroscopy (EIS). The aramid polymer and its coated form (Aramid@Zn) showed an ionic conductivity of 4.9



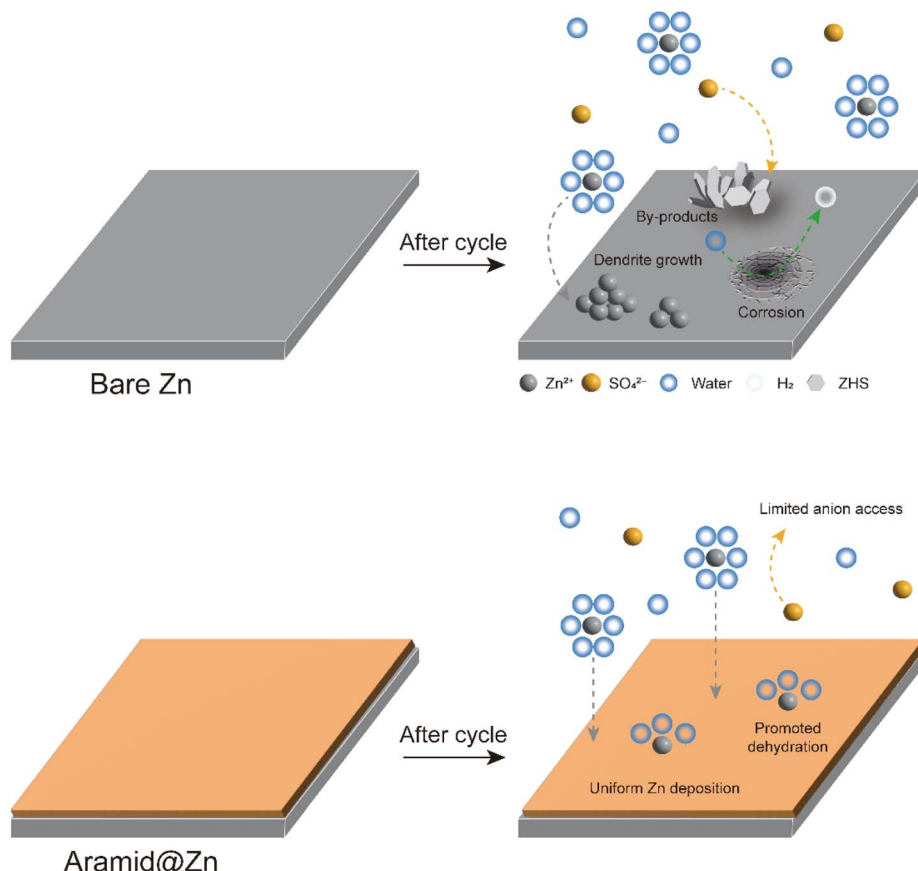


Fig. 1 Schematic illustration of Zn deposition behavior on Bare Zn and Aramid@Zn anodes.

$\times 10^{-4}$ S cm $^{-1}$ and 1.163×10^{-5} S cm $^{-1}$, respectively (Fig. S5, SI and 3a). Notably, this value is comparable to the conductivity of other protective interfacial layers reported in the literature, such as the ZCS layer formed in the presence of KPF₆ (1.403×10^{-5} S cm $^{-1}$).²⁷ The high ionic conductivity confirms that the aramid material effectively facilitates ion transport, likely owing to its molecular structure, including polar amide groups ($-\text{CONH}-$). These functional groups can provide favorable pathways for Zn²⁺ ions, promoting a stable and uniform ion transport across the interface between the electrolyte and electrode.²⁸

The interaction between the amide groups and Zn²⁺ ions was investigated using FT-IR and density functional theory (DFT) calculations. As shown in Fig. 3b, the amide mode, dominated by the C=O stretching band, shifted by ~ 8 cm $^{-1}$ to a lower energy after immersion in electrolyte for 24 h. This shift indicates a weakening of the C=O bond due to the interaction between Zn²⁺ ions and the carbonyl groups within the aramid backbone.^{29,30} DFT calculations confirm that the O atom is the most electron-rich and thus possibly the preferred Zn²⁺ binding site (Fig. S6, SI). As the Zn²⁺ ions strongly interact with the carbonyl groups, its dehydration process can be influenced by the aramid layer. Fig. 3c shows the energy penalty during the dehydration process with and without the aramid polymer, in reference to the fully hydrated complex, Zn²⁺(H₂O)₆. In an

aqueous solution without aramid, the Zn²⁺ ion becomes gradually unstable as dehydration proceeds, exhibiting an energy penalty of 2.20 eV in the middle of the dehydration process ($n = 2$). In contrast, when the Zn²⁺ ion interacts with a single aramid chain, the instability from dehydration is compensated for, as the aramid can occupy one coordination site, reducing the energy penalty to 1.42 eV for the $n = 2$ state. This effect is more enhanced when the Zn²⁺ ion interacts with two aramid chains, where it shows an energy penalty of only 0.64 eV for the $n = 2$. These results indicate that the aramid polymer network can promote the dehydration process of Zn²⁺ ions. To further confirm this, EIS measurements were carried out at different temperatures (Fig. S7, SI), and the activation energy (E_a) for desolvation was calculated using the Arrhenius equation. The E_a value of Aramid@Zn (33.4 kJ mol $^{-1}$) was lower than that of Bare Zn (40.3 kJ mol $^{-1}$) (Fig. 3d), indicating that the aramid layer facilitates the desolvation of hydrated Zn²⁺ ions.^{31,32}

Additional properties, such as Zn²⁺ transport and wettability of the aramid layer were examined. The Aramid@Zn anode exhibited a significantly higher Zn²⁺ transference number ($t_{\text{Zn}^{2+}}$) of 0.64, compared to 0.37 for the Bare Zn anode (Fig. S8, SI), indicating that the aramid layer enhances Zn²⁺ transport while restricting the migration of detrimental anions (e.g., SO₄²⁻ and OH⁻).^{29,33} This improvement suggests that the aramid layer not only facilitates Zn²⁺ diffusion but also mitigates the formation

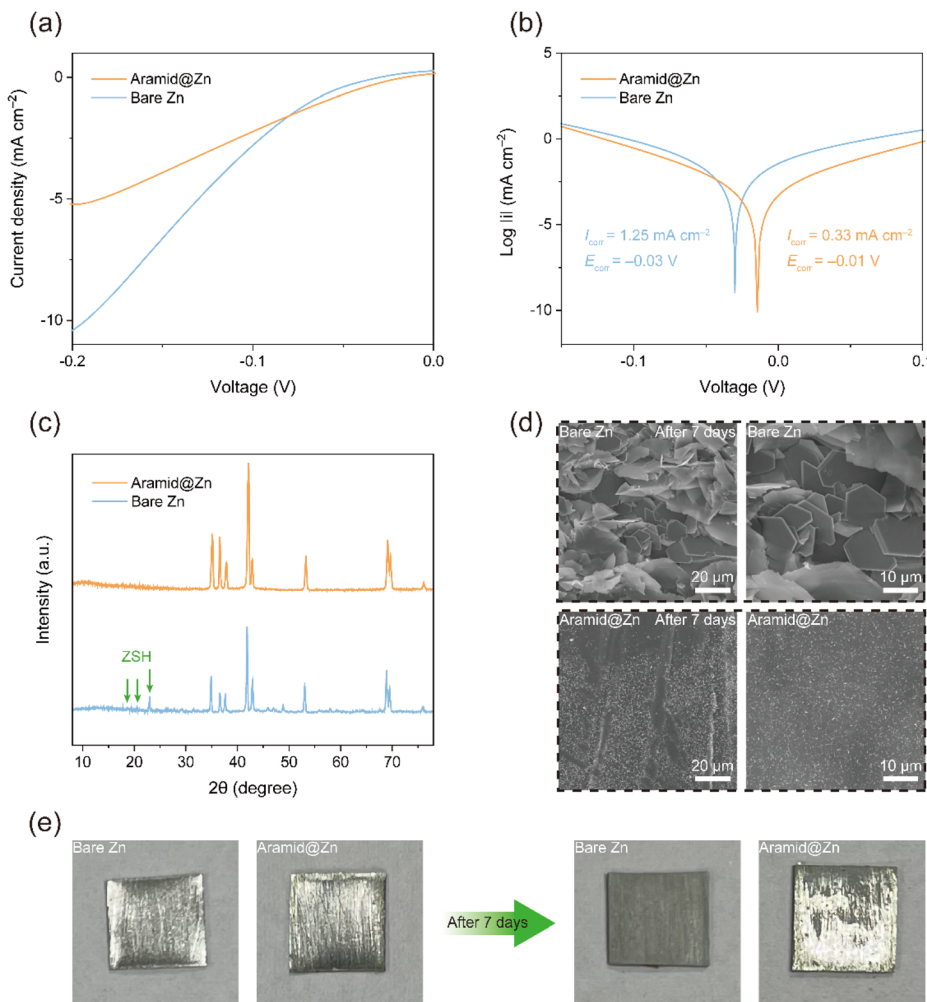


Fig. 2 (a) LSV curves of Bare Zn and Aramid@Zn anodes. (b) Linear polarization curves presenting the corrosion behavior of Bare Zn and Aramid@Zn anodes. (c) XRD pattern. (d) SEM images of Bare Zn and Aramid@Zn anodes after immersion in 2 M ZnSO_4 electrolyte for 7 days, shown at low magnification (left) and high magnification (right). (e) Digital photographs of Bare Zn and Aramid@Zn anodes before and after 7 days immersion in 2 M ZnSO_4 electrolyte.

of undesirable by-products by suppressing anion transport. The wettability of the Aramid@Zn surface was characterized using contact angle measurements (Fig. 3e). The Aramid@Zn exhibits a smaller contact angle (67°) compared to Bare Zn (89°), indicating that the amide groups enhance the wettability of the anodes. This improved wettability promotes the homogeneous dispersion of the electrolyte across the anode surface, facilitating Zn^{2+} ion transfer.³⁴

Based on these physical, electrochemical, and computational characterizations, Fig. 3f illustrates the operating mechanism of the aramid layer. The aramid layer, at its interface with the electrolyte, facilitates the access of Zn^{2+} ions while hindering the approach of anions. Subsequently, it assists the dehydration process of Zn^{2+} ions through coordination with carbonyl groups. Within the aramid layer, the transport of Zn^{2+} ions via these carbonyl groups is sufficiently fast and uniform, which in turn leads to the uniform electrodeposition of Zn metal.

Chronoamperometric (CA) analysis was employed to confirm this Zn^{2+} diffusion behavior using Zn symmetric cells (Fig. S9, SI). At an overpotential of -150 mV, the Bare Zn anode exhibited a continuous increase in current density over 300 s, indicating a rampant 2D diffusion process and excessive Zn deposition attributed to the “tip effect”, which drives dendrite growth.³⁵ Conversely, the Aramid@Zn anode achieved stable 3D diffusion after the initial Zn nucleation process, suggesting that the aramid layer effectively promotes uniform Zn deposition.

Electrochemical performance of the Aramid@Zn anode

$\text{Zn}||\text{Zn}$ symmetric cells were employed to evaluate the cycling performance of Bare Zn and Aramid@Zn anodes. The Aramid@Zn anode demonstrated outstanding cycling durability, maintaining stable performance for over 1000 h at 1 mA cm^{-2} with 1 mAh cm^{-2} (Fig. 4a). This exceptional cycling performance exceeds those of most previously reported $\text{Zn}||\text{Zn}$ symmetric cells (Table S2, SI). This result indicates that the



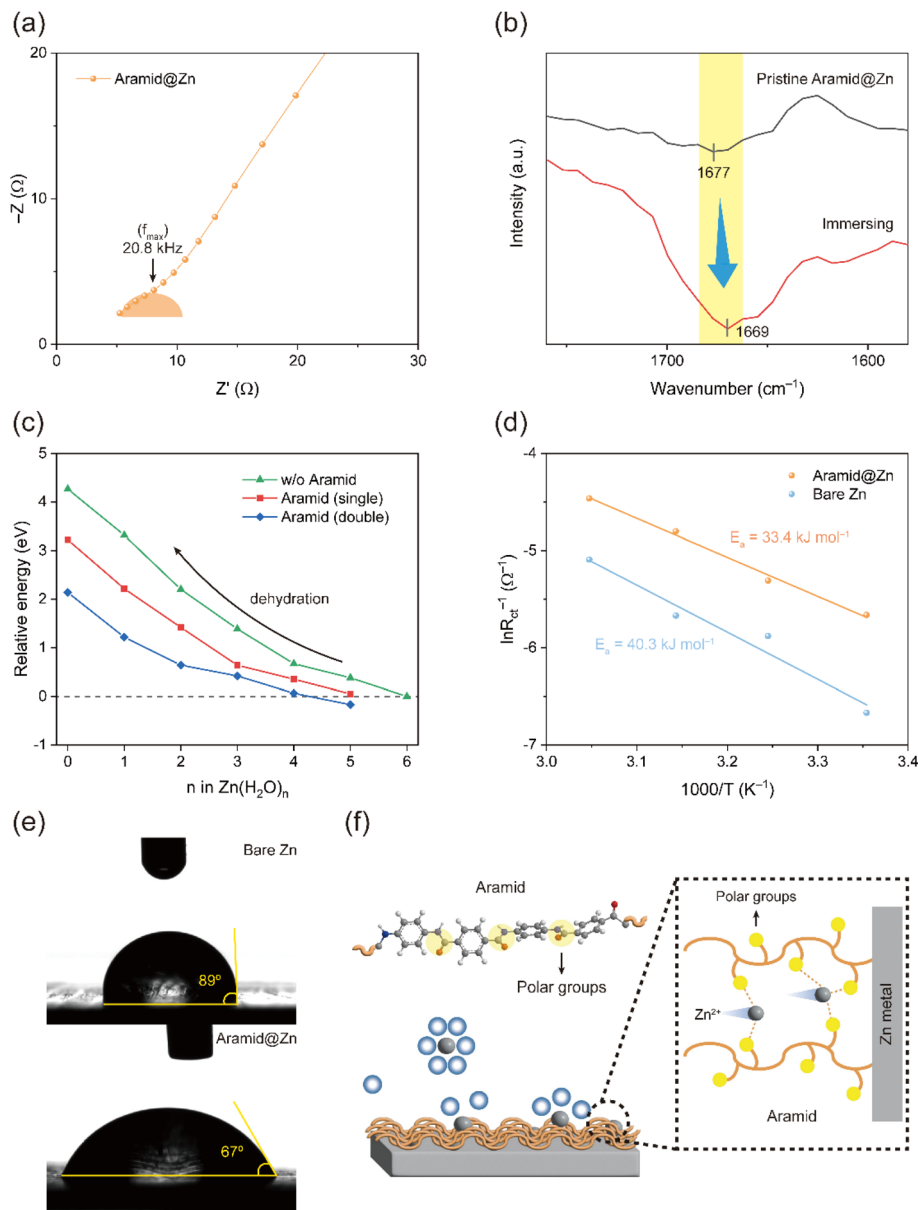


Fig. 3 (a) Enlarged EIS plot of Aramid@Zn symmetric cells. (b) FT-IR spectra of the aramid layer with/without immersing in 2 M ZnSO_4 electrolyte for 24 h. The spectra were shown in the range of 1600–1700 cm^{-1} to indicate the variation of $\text{C}=\text{O}$. (c) Relative energy of hydrated $\text{Zn}(\text{H}_2\text{O})_n$ complex with and without aramid chains in reference to the fully hydrated state ($n = 6$). (d) The activation energy of Bare Zn and Aramid@Zn anodes. (e) Contact angles of 2 M ZnSO_4 electrolyte on the Bare Zn and Aramid@Zn anodes. (f) Schematic illustration of ion-transport process in aramid polymer coating.

aramid coating effectively promotes uniform Zn^{2+} deposition while suppressing the Zn dendrite growth. In contrast, the Bare Zn anode exhibited significant voltage oscillation, leading to short-circuit failure within 100 h. Furthermore, the surface morphology of the electrodes was confirmed by scanning electron microscopy (SEM) after galvanostatic testing (Fig. S10, SI). While the polished Bare Zn surface displayed visible wear scar, the Aramid@Zn surface remained notably smoother due to the protective polymer layer. After 100 cycles, the Bare Zn electrode exhibited disorganized Zn dendrites, indicating uneven Zn^{2+} deposition and heterogeneous nucleation, which ultimately leads to capacity deterioration. Conversely, the aramid coating

significantly inhibited dendrite formation on the Aramid@Zn electrode, resulting in uniform deposition and nucleation of Zn^{2+} ions. At a high current density of 10 mA cm^{-2} , the Aramid@Zn anode maintained nearly 580 h (Fig. S11, SI). However, the Bare Zn anode experienced a short circuit after only 90 cycles due to uncontrolled dendrite growth, leading to cell failure.³⁶ In addition, testing at a higher areal capacity of 3 mAh cm^{-2} confirmed the enhanced stability of the Aramid@Zn anode (Fig. S12, SI).

Nucleation and deposition kinetics were further investigated by overpotential analysis. The reduced polarization observed for the Aramid@Zn anode (Fig. 4b) indicates a lower nucleation

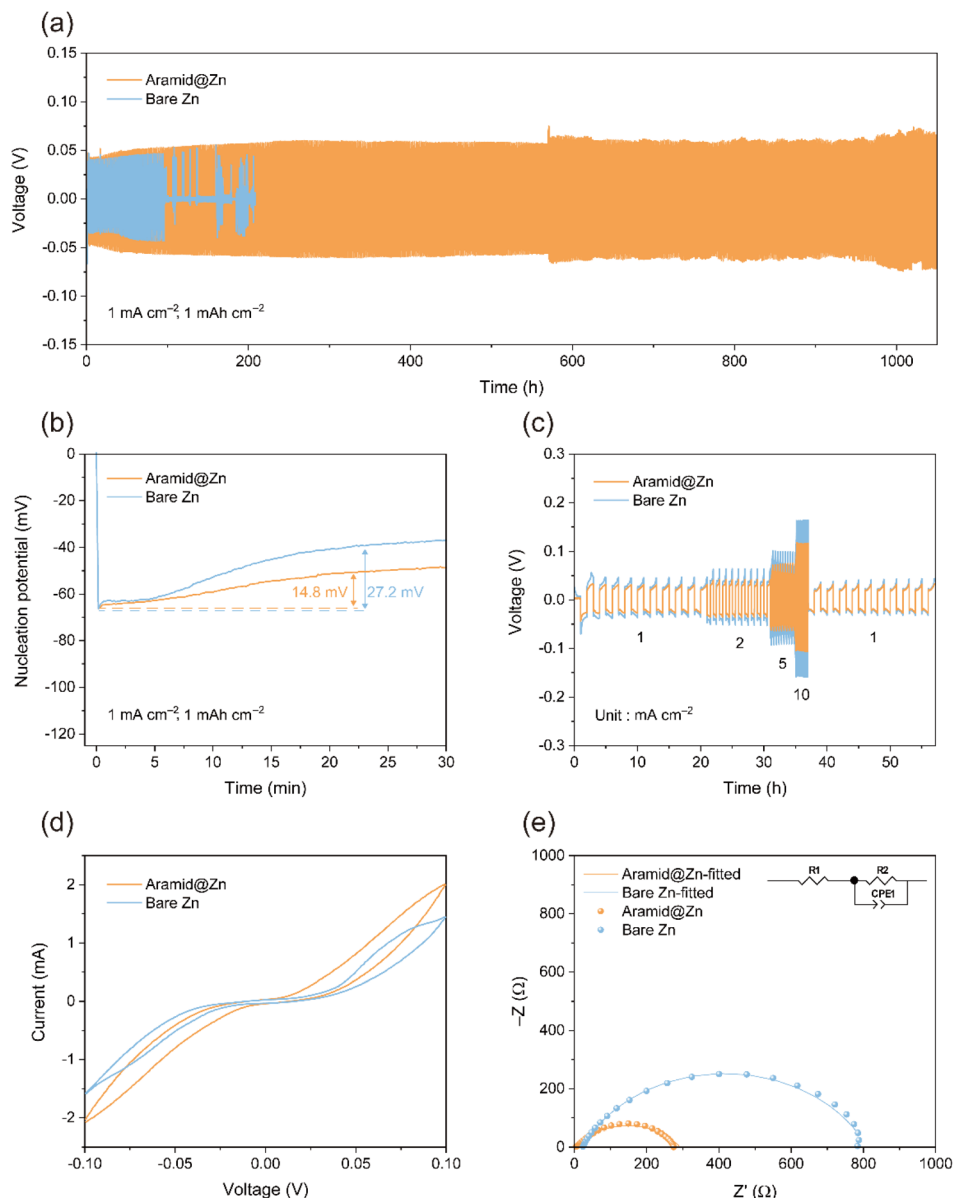


Fig. 4 (a) Long cycling performance and (b) nucleation overpotentials of the Zn symmetric cells at 1 mA cm^{-2} , 1 mAh cm^{-2} . (c) Rate performance of the Zn symmetric cells at a capacity of 1 mAh cm^{-2} . (d) Cyclic voltammetry (CV) curves of the Zn symmetric cells measured at 1 mV s^{-2} . (e) EIS plots of the symmetric cells before cycling.

energy barrier, attributed to zincophilic sites introduced by the aramid layer. These sites enhance the interaction between Zn^{2+} ions and the electrode interface, reducing the energy required for nucleation and growth. Rate performance of symmetric cells was evaluated across a range of current densities from 1 to 10 mA cm^{-2} , with a fixed areal capacity of 1 mAh cm^{-2} (Fig. 4c). The Aramid@Zn anode exhibited superior rate capability compared to the Bare Zn anode, demonstrating that the aramid coated Zn metal interphase significantly enhances the electrochemical performance by reducing the deposition energy barrier.

To evaluate the impact of interfacial reaction kinetics, cyclic voltammetry (CV) tests were conducted (Fig. 4d). Both the Bare Zn and Aramid@Zn anodes exhibited similar CV profiles,

indicating that the aramid coating does not alter the Zn^{2+}/Zn redox process. Moreover, the Aramid@Zn anode demonstrated a larger integrated peak area, suggesting an expanded electrochemically active region and enhanced Zn^{2+} concentration at the interface between the electrolyte and electrode. This contributes to improved Zn^{2+} transfer kinetics during the Zn stripping/plating process. In addition, the CV curves confirm the high reversibility of the Zn stripping/plating process.

Electrochemical impedance spectroscopy (EIS) was employed to evaluate the charge transfer resistance (R_{ct}) at the electrode/electrolyte interface (Fig. 4e). The Aramid@Zn anode exhibited a significantly lower R_{ct} of 287.7Ω compared to 786.8Ω for the Bare Zn anode, suggesting accelerated reaction kinetics at the Aramid@Zn anode/electrolyte interface. This

improvement is attributed to the presence of amide groups ($-\text{CONH}-$) in the aramid, facilitating faster interfacial reactions. Furthermore, to investigate the influence of coating thickness on interfacial stability, EIS measurements were performed using coating layers with thicknesses of approximately 8, 14, and 24 μm . As shown in Fig. S13(SI), the 14 μm coating exhibited the most stable interfacial resistance. This result indicates that a thin coating may not uniformly cover the entire electrode surface, while a thick layer could hinder Zn^{2+} ion transport.

To assess the reversibility of Zn stripping/plating, coulombic efficiency (CE) was evaluated in $\text{Zn}||\text{Cu}$ asymmetric cells under conditions of 1 mA cm^{-2} and 0.5 mAh cm^{-2} (Fig. S14a, SI). The Bare Zn anode displayed fluctuating CE behavior and failed rapidly to sustain reversible Zn plating due to side reactions. In contrast, the CE of the Aramid@Zn||Cu cell was still 98.5% after 125 cycles, indicating excellent cycling stability. In addition, the cell exhibited a consistent capacity–voltage profile and low voltage polarization throughout cycling (Fig. S14b, SI). These results suggest that the aramid coating effectively suppresses side reactions, thereby enhancing the reversibility and stability of the Zn anode during cycling.

In AZIBs, repeated cycling leads to an increase in internal temperature due to increased resistance and electrochemical reactions. This temperature rise accelerates performance degradation, primarily driven by Zn corrosion and dendrite formation. At elevated temperatures, Zn reacts with the electrolyte, releasing hydrogen gas and forming non-conductive by-products on the electrode surface.³⁷ These reactions compromise the stability of the Zn anode interface, increase internal resistance, and reduce electrode lifespan. To mitigate performance degradation caused by temperature rise during cycling, a protection strategy that maintains stability at high temperatures is essential.

The Aramid@Zn anode offers a robust protective barrier, suppressing Zn corrosion and controlling dendrite growth under elevated temperatures. To elucidate the stabilizing effects of the aramid coating on Zn anodes under thermal stress, symmetrical cell cycling tests were performed at 55 °C to evaluate its impact on Zn deposition behavior and overpotential characteristics. As shown in Fig. S15(SI), the Bare Zn anode exhibited a prominent voltage dip at each cycle onset, indicative of a high nucleation overpotential. Such elevated nucleation overpotentials are known to lead to non-uniform Zn deposition, often resulting in dendritic structures and surface irregularities.³⁸ Furthermore, an increasing polarization trend in the latter stages of each cycle highlighted the progressively more energy-intensive stripping process, suggesting surface inhomogeneities. In contrast, the Aramid@Zn anode displayed no observable nucleation overpotential dips over successive cycles and maintained a higher plateau polarization. This behavior indicates that the aramid coating acts as an effective barrier, mitigating dendritic growth and undesirable side reactions exacerbated by high temperatures.

Further analysis by XRD revealed that, at high temperature, the Bare Zn anode undergoes intensified side reactions, leading to significant by-product formation (Fig. S16, SI). SEM images

(Fig. S17, SI) corroborated this observation, displaying the Zn dendrite flakes on the Bare Zn surface, a morphology associated with unstable Zn deposition. In contrast, the Aramid@Zn anode exhibited minimal morphological changes, indicating that the aramid coating provides an effective barrier against high temperature degradation. These combined results demonstrate that the aramid coating not only reduces interfacial resistance but also inhibits temperature-induced side reactions and dendrite formation, thereby enhancing the stability and performance of the Zn anode under thermal stress conditions.

Electrochemical performance of $\text{Zn}||\alpha\text{-MnO}_2$ full cells

The full cells were assembled to further verify the effect of the Aramid@Zn anode on battery performance. The full cells were composed of an $\alpha\text{-MnO}_2$ cathode and $2 \text{ M ZnSO}_4 + 0.1 \text{ M MnSO}_4$ electrolyte for electrochemical evaluation. The $\alpha\text{-MnO}_2$ cathode was synthesized by a hydrothermal method, and the corresponding XRD pattern and SEM images are presented in Fig. S18(SI) and S19(SI), respectively. Based on the XRD analysis, $\alpha\text{-MnO}_2$ crystallizes in the tetragonal phase with the space group I_4/m .^{39,40} The refined lattice parameters are summarized in Table S1(SI).

Fig. 5a presents the CV curves of $\text{Zn}||\alpha\text{-MnO}_2$ and Aramid@Zn|| $\alpha\text{-MnO}_2$ full cells at a scan rate of 0.1 mV s^{-1} in a voltage window between 0.8 and 1.9 V. Two pairs of characteristic redox peaks were observed in the CV curves for both Aramid@Zn|| $\alpha\text{-MnO}_2$ and Bare Zn|| $\alpha\text{-MnO}_2$ cells, consistent with previous findings in the literature.⁴¹ Compared to the Bare Zn|| $\alpha\text{-MnO}_2$ cell, the Aramid@Zn|| $\alpha\text{-MnO}_2$ cell exhibited higher current intensity and lower voltage polarization, indicating enhanced electrochemical reactivity and reaction kinetics facilitated by the aramid coating. As a result, the Aramid@Zn anode demonstrated an increased current response in the full cell compared to the Bare Zn anode, suggesting a higher capacity value, as validated by the galvanostatic charge–discharge (GCD) curves in Fig. 5b. Additionally, the charge–discharge plateaus of the Aramid@Zn|| $\alpha\text{-MnO}_2$ cell were comparable to those of the Bare Zn|| $\alpha\text{-MnO}_2$ cell, indicating that the Aramid coating maintains the intrinsic redox process while enhancing reaction kinetics and capacity retention. This phenomenon was validated by the rate performance of full cells at various current densities ranging from 0.1 to 2 A g^{-1} , as shown in Fig. 5c, where the Aramid@Zn|| $\alpha\text{-MnO}_2$ cell exhibited significantly higher discharge capacities across all tested current densities. The enhanced performance can be attributed to the aramid coating, which facilitates Zn^{2+} transport. These findings are consistent with the CV results, where reduced voltage polarization and higher current intensity were observed for the Aramid@Zn|| $\alpha\text{-MnO}_2$ cell, underscoring the role of the aramid coating in achieving superior electrochemical performance and stability under high rate conditions.^{42,43}

As depicted in Fig. 5d, the Aramid@Zn|| $\alpha\text{-MnO}_2$ cell exhibits a discharge capacity of 209 mAh g^{-1} after 100 cycles at 0.1 A g^{-1} , outperforming the Bare Zn|| $\alpha\text{-MnO}_2$ cell, which retains only 184 mAh g^{-1} . This improved capacity retention demonstrates the enhanced cycling stability provided by the aramid coating. To



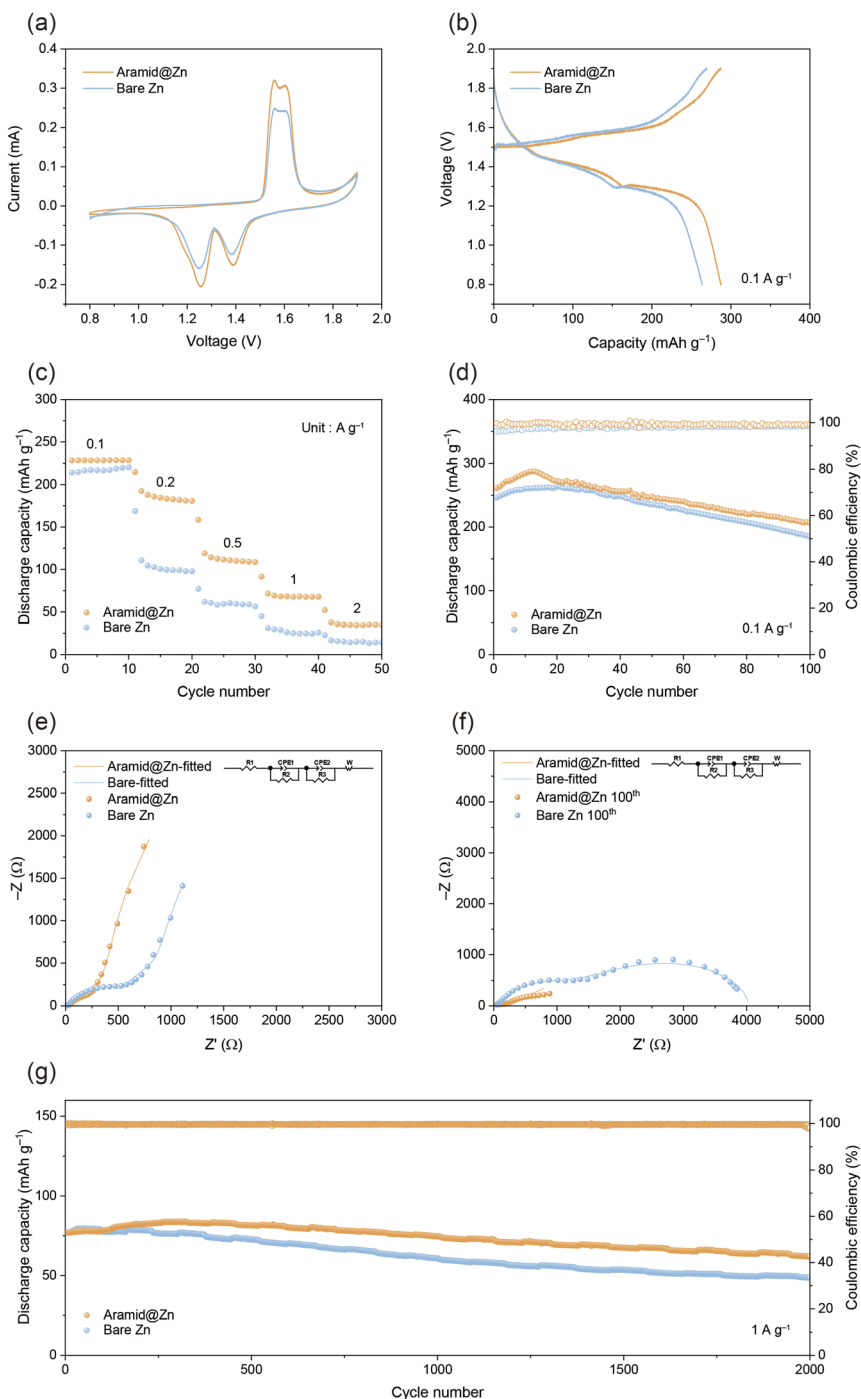


Fig. 5 $\text{Zn}||\alpha\text{-MnO}_2$ full cells with Bare Zn and Aramid@Zn anodes. (a) CV curves at a scan rate of 0.1 mV s^{-1} . (b) Galvanostatic charge–discharge curves at 0.1 A g^{-1} . (c) Rate performance at current densities ranging from 0.1 to 2 A g^{-1} . (d) Cycling performance at 0.1 A g^{-1} . (e) EIS plots of the full cells before cycling and (f) after 100 cycles. (g) Cycling performance at 1 A g^{-1} .

further investigate the interfacial stability of electrodes, EIS was conducted before and after 100 cycles. Before cycling, the Aramid@Zn anode exhibited a lower R_{ct} of 200.2Ω , confirming that the aramid coating effectively inhibits side reactions and promotes controlled Zn deposition compared to Bare Zn anode (513.7Ω) (Fig. 5e). After 100 cycles, EIS measurements were repeated to assess the long-term stability of the interfacial layer provided by the aramid coating (Fig. 5f). For the Bare Zn anode,

the surface film resistance (R_{sf}) and R_{ct} values were significantly higher, measured at 983.4Ω and 4141Ω , respectively, indicating the formation of a resistive interfacial layer and increased charge transfer impedance due to side reactions and surface degradation. In contrast, the Aramid@Zn anode maintained lower R_{sf} and R_{ct} values of 129.7Ω and 991.6Ω , respectively, suggesting that the aramid layer effectively stabilizes the interface by suppressing side reactions and promoting efficient

ion and electron transfer.^{29,44} The improved interfacial stability of the Aramid@Zn anode contributed to the prolonged cycling stability observed in the full cells. This stabilization became more evident under high rate cycling conditions. When tested at 1 A g^{-1} (Fig. 5g), the Aramid@Zn|| α -MnO₂ cell retained 80.2% of its capacity after 2000 cycles. In contrast, the Bare Zn|| α -MnO₂ cell suffered from severe capacity fading, retaining only 63.2% under the same conditions. These results highlight the effectiveness of the aramid coating in suppressing side reactions and enhancing the long-term stability.

Conclusions

In this investigation, we demonstrate that an aramid coating significantly enhances the electrochemical performance and stability of Zn anodes in AZIBs. By suppressing dendrite formation, reducing side reactions, and mitigating interfacial charge transfer resistance, the aramid coating stabilizes the Zn surface, as confirmed by EIS and XRD analyses. Symmetric cell tests reveal the remarkable cycling durability of the Aramid@Zn anode, sustaining over 1000 h of stable operation with minimal degradation. Zn|| α -MnO₂ full cells achieve exceptional capacity retention of 80.2% after 2000 cycles, demonstrating superior long-term performance. Notably, the aramid coating exhibits robust resistance to thermal stress, effectively suppressing side reactions such as hydrogen evolution and by-product formation, as well as inhibiting dendrite growth, even under elevated temperature conditions. These findings collectively establish the potential of aramid coating as a promising solution for overcoming the challenges of Zn anodes, advancing the development of durable, high performance AZIBs for energy storage applications. Furthermore, the coating process is compatible with roll-to-roll, solution-based techniques, which highlights its scalability and potential for seamless integration into existing battery manufacturing lines. These advantages collectively establish the aramid coating as a practical, commercially viable strategy for next-generation AZIBs.

Conflicts of interest

There are no conflicts to declare.

Data availability

The data supporting this article have been included as part of the SI.

Additional experimental details, calculation methods, and characterization data (XRD, SEM, EIS, etc.), as well as supplementary figures, tables, and supporting discussion referenced in the main text. See DOI: <https://doi.org/10.1039/d5ta03948g>.

Acknowledgements

This work was supported by the National Research Foundation of Korea (NRF) grant funded by the Korea government (MSIT) (No. RS-2022-NR071869 and RS-2025-02215502). H. K.

acknowledges support from the Korea Basic Science Institute (PG2025008).

References

- 1 T. Chen, Y. Jin, H. Lv, A. Yang, M. Liu, B. Chen, Y. Xie and Q. Chen, Applications of lithium-ion batteries in grid-scale energy storage systems, *Trans. Tianjin Univ.*, 2020, **26**(3), 208–217.
- 2 R. Zhang, X. Shi, O. C. Esan and L. An, Organic electrolytes recycling from spent lithium-ion batteries, *Global Challenges*, 2022, **6**(12), 2200050.
- 3 J. Kalhoff, G. G. Eshetu, D. Bresser and S. Passerini, Safer electrolytes for lithium-ion batteries: state of the art and perspectives, *ChemSusChem*, 2015, **8**(13), 2154–2175.
- 4 Q. Wang, L. Jiang, Y. Yu and J. Sun, Progress of enhancing the safety of lithium ion battery from the electrolyte aspect, *Nano Energy*, 2019, **55**, 93–114.
- 5 J. Ming, J. Guo, C. Xia, W. Wang and H. N. Alshareef, Zinc-ion batteries: Materials, mechanisms, and applications, *Mater. Sci. Eng., R*, 2019, **135**, 58–84.
- 6 M. Iturrondobeitia, O. Akizu-Gardoki, O. Amondarain, R. Minguez and E. Lizundia, Environmental impacts of aqueous zinc ion batteries based on life cycle assessment, *Adv. Sustainable Syst.*, 2022, **6**(1), 2100308.
- 7 H. Lu, J. Hu, X. Wei, K. Zhang, X. Xiao, J. Zhao, Q. Hu, J. Yu, G. Zhou and B. Xu, A recyclable biomass electrolyte towards green zinc-ion batteries, *Nat. Commun.*, 2023, **14**(1), 4435.
- 8 S. Liu, L. Kang, J. M. Kim, Y. T. Chun, J. Zhang and S. C. Jun, Recent advances in vanadium-based aqueous rechargeable zinc-ion batteries, *Adv. Energy Mater.*, 2020, **10**(25), 2000477.
- 9 K. LOLUPIMA, J. Cao, D. ZHANG, C. YANG, X. ZHANG and J. QIN, A review on the development of metals-doped Vanadium oxides for zinc-ion battery, *J. Met., Mater. Miner.*, 2024, **34**(3), 2084.
- 10 L. Zhuo, T. T. BEYENE, Z. Kai and C. Dianxue, Realizing fast plating/stripping of high-performance Zn metal anode with a low Zn loading, *J. Met., Mater. Miner.*, 2024, **34**(2), 2009.
- 11 T. Mawintorn, K. Lolupiman, N. Kiatwisarnkij, P. Woottapanit, M. Karnan, S. S. N. Ayuttay, X. Zhang, P. Wangyao and J. Qin, Fabrication and characterization of zinc anode on nickel conductive cloth for high-performance zinc ion battery applications, *J. Met., Mater. Miner.*, 2024, **34**(3), 2083.
- 12 N. Kiatwisarnkij, Z. Song, C. Tangpongkitjaroen, S. Wannapaiboon, X. Zhang, P. Wangyao and J. Qin, Texturing (002)-Oriented Zinc Atop a Cotton Cloth for High-Performance Zn-Ion Batteries, *Batteries Supercaps*, 2025, e202400727.
- 13 P. Tanapornchinpong, C.-W. Yang, Y.-H. Zhao, N. Kiatwisarnkij, K. Lolupiman, S. Rajendran, Y.-P. Lei, X.-Y. Zhang, P. Wangyao and J.-Q. Qin, Enhanced Zn plating and stripping behavior of the utilized fly ash-coated Zn anode for zinc-ion batteries, *Rare Met.*, 2025, **44**(7), 4621–4630.
- 14 C. Nie, G. Wang, D. Wang, M. Wang, X. Gao, Z. Bai, N. Wang, J. Yang, Z. Xing and S. Dou, Recent Progress on Zn Anodes



for Advanced Aqueous Zinc-Ion Batteries, *Adv. Energy Mater.*, 2023, **13**(28), 2300606.

15 D. Wang, Q. Li, Y. Zhao, H. Hong, H. Li, Z. Huang, G. Liang, Q. Yang and C. Zhi, Insight on organic molecules in aqueous Zn-ion batteries with an emphasis on the Zn anode regulation, *Adv. Energy Mater.*, 2022, **12**(9), 2102707.

16 Y. Zhang, X. Han, R. Liu, Z. Yang, S. Zhang, Y. Zhang, H. Wang, Y. Cao, A. Chen and J. Sun, Manipulating the zinc deposition behavior in hexagonal patterns at the preferential Zn (100) crystal plane to construct surficial dendrite-free zinc metal anode, *Small*, 2022, **18**(7), 2105978.

17 N. Zhang, X. Chen, M. Yu, Z. Niu, F. Cheng and J. Chen, Materials chemistry for rechargeable zinc-ion batteries, *Chem. Soc. Rev.*, 2020, **49**(13), 4203–4219.

18 J. Kim, J. Oh and H. Lee, Review on battery thermal management system for electric vehicles, *Appl. Therm. Eng.*, 2019, **149**, 192–212.

19 G. Liu, M. Ouyang, L. Lu, J. Li and X. Han, Analysis of the heat generation of lithium-ion battery during charging and discharging considering different influencing factors, *J. Therm. Anal. Calorim.*, 2014, **116**, 1001–1010.

20 P. Yang, C. Feng, Y. Liu, T. Cheng, X. Yang, H. Liu, K. Liu and H. J. Fan, Thermal self-protection of zinc-ion batteries enabled by smart hygroscopic hydrogel electrolytes, *Adv. Energy Mater.*, 2020, **10**(48), 2002898.

21 J. Zhou, M. Xie, F. Wu, Y. Mei, Y. Hao, R. Huang, G. Wei, A. Liu, L. Li and R. Chen, Ultrathin surface coating of nitrogen-doped graphene enables stable zinc anodes for aqueous zinc-ion batteries, *Adv. Mater.*, 2021, **33**(33), 2101649.

22 R. Ramani, T. Kotresh, R. I. Shekar, F. Sanal, U. Singh, R. Renjith and G. Amarendra, Positronium probes free volume to identify para-and meta-aramid fibers and correlation with mechanical strength, *Polymer*, 2018, **135**, 39–49.

23 M. Zhou, Y. Chen, G. Fang and S. Liang, Electrolyte/electrode interfacial electrochemical behaviors and optimization strategies in aqueous zinc-ion batteries, *Energy Storage Mater.*, 2022, **45**, 618–646.

24 J. L. Yang, J. Li, J. W. Zhao, K. Liu, P. Yang and H. J. Fan, Stable zinc anodes enabled by a zincophilic polyanionic hydrogel layer, *Adv. Mater.*, 2022, **34**(27), 2202382.

25 Y. Mao, Z. Li, Y. Li, D. Cao, G. Wang, K. Zhu and G. Chen, Breaking intramolecular hydrogen bonds of polymer films to enable dendrite-free and hydrogen-suppressed zinc metal anode, *Chem. Eng. J.*, 2023, **461**, 141707.

26 Y. Zhou, G. Li, S. Feng, H. Qin, Q. Wang, F. Shen, P. Liu, Y. Huang and H. He, Regulating Zn ion desolvation and deposition chemistry toward durable and fast rechargeable Zn metal batteries, *Adv. Sci.*, 2023, **10**(6), 2205874.

27 Y. Chu, S. Zhang, S. Wu, Z. Hu, G. Cui and J. Luo, In situ built interphase with high interface energy and fast kinetics for high performance Zn metal anodes, *Energy Environ. Sci.*, 2021, **14**(6), 3609–3620.

28 C. Zhang, X. Qian, D. Wang, C. Chen, Y. Chen, T. Chen and J. Fu, Building ion-conductive supramolecular elastomeric protective layer *via* dynamic hard domain design for stable zinc metal anodes, *ACS Appl. Mater. Interfaces*, 2023, **15**(41), 48185–48195.

29 Z. Zhao, J. Zhao, Z. Hu, J. Li, J. Li, Y. Zhang, C. Wang and G. Cui, Long-life and deeply rechargeable aqueous Zn anodes enabled by a multifunctional brightener-inspired interphase, *Energy Environ. Sci.*, 2019, **12**(6), 1938–1949.

30 Y. Geng, W. Xin, L. Zhang, Y. Han, H. Peng, M. Yang, H. Zhang, X. Xiao, J. Li and Z. Yan, Building electrode/electrolyte interphases in aqueous zinc batteries *via* self-polymerization of electrolyte additives, *Natl. Sci. Rev.*, 2025, **12**(1), nwae397.

31 M. Chen, X. Guo, X. Jiang, B. Farhadi, X. Guo, Y. Zhu, H. Zhang and S. Liu, Multi-Group Polymer Coating on Zn Anode for High Overall Conversion Efficiency Photorechargeable Zinc-Ion Batteries, *Angew. Chem., Int. Ed.*, 2024, **63**(39), e202410011.

32 S. Wu, S. Zhang, Y. Chu, Z. Hu and J. Luo, Stacked Lamellar Matrix Enabling Regulated Deposition and Superior Thermo-Kinetics for Advanced Aqueous Zn-Ion System under Practical Conditions, *Adv. Funct. Mater.*, 2021, **31**(49), 2107397.

33 Z. Xing, Y. Sun, X. Xie, Y. Tang, G. Xu, J. Han, B. Lu, S. Liang, G. Chen and J. Zhou, Zincophilic electrode interphase with appended proton reservoir ability stabilizes Zn metal anodes, *Angew. Chem., Int. Ed.*, 2023, **62**(5), e202215324.

34 Q. Yang, Q. Li, Z. Liu, D. Wang, Y. Guo, X. Li, Y. Tang, H. Li, B. Dong and C. Zhi, Dendrites in Zn-based batteries, *Adv. Mater.*, 2020, **32**(48), 2001854.

35 D. Xie, Z. W. Wang, Z. Y. Gu, W. Y. Diao, F. Y. Tao, C. Liu, H. Z. Sun, X. L. Wu, J. W. Wang and J. P. Zhang, Polymeric molecular design towards horizontal Zn electrodeposits at constrained 2D Zn^{2+} diffusion: dendrite-free Zn anode for long-life and high-rate aqueous zinc metal battery, *Adv. Funct. Mater.*, 2022, **32**(32), 2204066.

36 Z. Hou, Y. Gao, R. Zhou and B. Zhang, Unraveling the rate-dependent stability of metal anodes and its implication in designing cycling protocol, *Adv. Funct. Mater.*, 2022, **32**(7), 2107584.

37 H. He, H. Qin, F. Shen, N. Hu and J. Liu, Low temperature induced highly stable Zn metal anodes for aqueous zinc-ion batteries, *Chem. Commun.*, 2021, **57**(87), 11477–11480.

38 M. Kim, J. Lee, Y. Kim, Y. Park, H. Kim and J. W. Choi, Surface overpotential as a key metric for the discharge-charge reversibility of aqueous zinc-ion batteries, *J. Am. Chem. Soc.*, 2023, **145**(29), 15776–15787.

39 D. Gangwar and C. Rath, Structural, optical and magnetic properties of α -and β -MnO₂ nanorods, *Appl. Surf. Sci.*, 2021, **557**, 149693.

40 R. Lan, E. Gkanas, A. J. S. Sahib, A. Greszta, R. Bhagat and A. Roberts, The effect of copper doping in α -MnO₂ as cathode material for aqueous Zinc-ion batteries, *J. Alloys Compd.*, 2024, **992**, 174528.

41 J. Hao, B. Li, X. Li, X. Zeng, S. Zhang, F. Yang, S. Liu, D. Li, C. Wu and Z. Guo, An in-depth study of Zn metal surface chemistry for advanced aqueous Zn-ion batteries, *Adv. Mater.*, 2020, **32**(34), 2003021.



42 J. Zou, Z. Zeng, C. Wang, X. Zhu, J. Zhang, H. Lan, L. Li, Y. Yu, H. Wang and X. Zhu, Ultraconformal Horizontal Zinc Deposition toward Dendrite-Free Anode, *Small Struct.*, 2023, **4**(1), 2200194.

43 R. Zhao, H. Wang, H. Du, Y. Yang, Z. Gao, L. Qie and Y. Huang, Lanthanum nitrate as aqueous electrolyte additive for favourable zinc metal electrodeposition, *Nat. Commun.*, 2022, **13**(1), 3252.

44 T. Sattar, S.-J. Sim, B.-S. Jin and H.-S. Kim, Dual function Li-reactive coating from residual lithium on Ni-rich NCM cathode material for Lithium-ion batteries, *Sci. Rep.*, 2021, **11**(1), 18590.

